

NEURONAL RESILIENCE AND CALCIUM SIGNALING PATHWAYS IN THE CONTEXT OF SYNAPSE LOSS AND CALCIUM LEAKS: A COMPUTATIONAL MODELLING STUDY AND IMPLICATIONS FOR ALZHEIMER'S DISEASE*

PIYUSH BOROLE[†], JAMES M. ROSADO[‡], MEIROSE NEAL[‡], AND GILLIAN QUEISSER[‡]

Abstract. In this paper a coupled electro-calcium model was developed and implemented to computationally explore the effects of neuronal synapse loss, in particular in the context of Alzheimer's disease. Established parameters affected by Alzheimer's disease, such as synapse loss, calcium leaks at deteriorating synaptic contacts, and downregulation of the calcium-buffer Calbindin, are subject to this study. Reconstructed neurons are used to define the computational domain for a system of partial and ordinary differential equations, discretized by finite differences and solved with a semi-implicit second order time integrator. The results show neuronal resilience during synapse loss. When incorporating calcium leaks at affected synapses, neurons lose their ability to produce synapse to nucleus calcium signals, necessary for learning, plasticity, and neuronal survival. Down-regulation of Calbindin concentrations partially recovers the signaling pathway to the cell nucleus. These results could define future research pathways towards stabilizing the calcium signaling pathways during Alzheimer's disease. The coupled electro-calcium model was implemented and solved using Matlab.

Key words. Multiscale Modeling, Neurons, Calcium, Dendrites, Synapse Loss, Amyloid β , Hodgkin-Huxley, Plasticity, Numerical Analysis, Alzheimer's Disease

AMS subject classifications. 92-10, 00A69, 65K05, 92C20

1. Introduction. Degeneration of neuronal signaling due to ageing and neuropathologies, such as Alzheimer's and Parkinson's disease [65, 5, 4, 67, 35, 1, 15, 22, 47, 92, 14], has become a very important research area. During ageing, or due to pathologies, changes in synaptic information transfer and intracellular responses to neuronal network communication disrupt the finely regulated intracellular signaling cascades, that enable neurons to control gene transcription responses [4, 24]. These responses have been shown to affect learning, cellular plasticity, neuronal health, and cell survival [5, 64, 69, 79]. Intracellular calcium signaling has been shown to play an outsized role in regulating information transfer from synaptic sites to the cell nucleus [38, 39, 36, 20], which harbors the DNA. Disruption of calcium signals, induced by neurodegenerative diseases, is implicated in neuronal decay and onset of clinical symptoms [51, 74]. Taking Alzheimer's disease (AD) as an example, accumulation of amyloid- β proteins at chemical synapses disrupts synaptic communication [89, 98, 84, 49, 66], as well as the intracellular calcium machinery. Calcium leaks [22, 47, 23, 63, 52, 78, 25, 26, 57], changes in ryanodine-receptor (RyR) activity, which causes increased calcium release from the endoplasmic reticulum (ER) into the cytosol [86], as well as reduction of the calcium-buffering molecule calbindin [46, 55, 17, 71], are all consequences of Alzheimer-induced degeneration.

Since systematic experimental modifications of the calcium machinery, e.g., local changes in the RyR density, the morphology of the ER, or synaptic activation patterns, are extremely hard, if not impossible, to carry out, we decided to develop a computational model that couples an electrical model for ion channel dynamics on the neuronal plasma membrane (PM) with a detailed calcium model that describes the

*Submitted to the editors August 12, 2025

[†]University of Edinburgh, Edinburgh, Scotland, United Kingdom

[‡]Department of Mathematics, Temple University, Philadelphia, Pennsylvania, U.S.A.

intracellular calcium dynamics governed by PM-exchange mechanisms, store release and sequestration from the ER, and diffusion-reaction processes in the cytosol. Using this model, we then studied calcium dynamics in unmodified, healthy, neurons and compared these to neuropathological states, defined by synapse loss, calcium leaks in the PM, changes in ER refilling, and buffering (cytosolic and ER) capacities.

The focus of this study was to understand the impact of AD pathologies on Ca^{2+} signaling in neurons. Previously, calcium models have been used to study parameters associated with stable and abortive Ca^{2+} waves [11, 12, 80] in neuronal sub-compartments. Models using full neuron geometries have been used to study electrical dynamics and action potential generation [87, 95]. Repeated synaptic events need to translate into rapid Ca^{2+} release from the ER into the cytosol to initiate stable Ca^{2+} signals. This, in turn, requires rapid ER refilling mechanisms. One such mechanism is governed by store-operated-calcium-channels (SOC), which support ER refilling. SOC models have been developed in [68, 32]. Additionally, the ER lumen stores vast amounts of Ca^{2+} in buffered form. Buffering dynamics in the ER have been modeled in [40]. Calcium leaks associated with amyloid- β have been studied in [60, 19]. As described previously, another pathology associated with AD is synapse loss which has been studied using neuronal network models [50, 93]. Dave et al. [18] implemented a 3D calcium model and tested the impact of Ca^{2+} buffer concentrations on Ca^{2+} signaling. While these models address individual calcium-regulators, we here developed an integrated electro-calcium model to simulate full-cell dynamics from synapse to cell nucleus.

The biophysical model is solved numerically on computational domains, using detailed morphological reconstructions, available on NeuroMorpho.org [3]. To efficiently solve the bidirectionally coupled electro-calcium model, we discretize the computational domain using finite differences and use the multistep implicit-explicit (ImEx) method known as SBDF2 (second order semi-implicit backward differentiation), [83, 2] as a time-integrator. We implement a dimensionally reduced set of model equations by way of rotational symmetry of the dendritic branches.

The paper is organized as follows: In Sec. 2 we derive the calcium model, consisting of all relevant calcium-exchange mechanisms, and couple this model to a Hodgkin-Huxley electrical model through voltage-dependent calcium channels (VDCCs). We then detail the process of integrating reconstructed neuron geometries into our numerical simulations, as well as the numerical methods. In Sec. 3 we detail the results from systematically changing parameters relevant in neurodegeneration, followed by a discussion in Sec. 4.

Using our computational framework we were able to show that neurons are capable of generating calcium waves towards the nucleus even under conditions of synapse loss, as seen during AD. Here, lost synapses are classified as no longer active in producing a postsynaptic calcium influx. If, however, those sites become leaky for calcium, a previously reported phenomenon [22, 47, 23, 63, 52, 78, 25, 26, 57], calcium communication between synapses and soma breaks down if the neuron experiences roughly 50% synapse loss or more. A reduction in the concentration of the calcium buffering molecule calbindin, an effect of AD [46, 55, 17, 71], counters the effect of leaky (and lost) synapses to a certain degree. Based on the presented work it appears that neurons are equipped to compensate a substantial loss of synapses with respect to synapse to nucleus communication. It is the leakiness of deteriorating synapses that causes a collapse of robust calcium signaling.

2. The Biophysical Model and Numerical Methods. In this section we derive and describe all model equations, cell geometry integration, and numerical methods for solving the coupled electro-calcium model.

2.1. Model Equations. In this section we discuss the model equations that are used to describe intracellular ion signaling and plasma membrane electrical signal propagation. The spatio-temporal ion dynamics are modeled by a system of diffusion-reaction equations, found in [11, 12], and are of the form

$$(2.1) \quad \frac{\partial u}{\partial t} = D\Delta u + R(u),$$

which were adapted for 1D neuronal geometries, by assuming rotational symmetry. Here, u denotes ion concentration, D the corresponding diffusion coefficient, and $R(u)$ a reaction term. We used the Hodgkin-Huxley model (HH) equations [37, 41, 42, 43, 44, 45] for electrical signal dynamics, with sodium (Na^+), potassium (K^+), calcium (Ca^{2+}), and leak ion channel dynamics. We coupled the electrical dynamics with spatio-temporal ions dynamics by including voltage dependent calcium channels (VDCCs) on the plasma membrane. A *feed forward* coupling, in which the membrane potential drives the release of calcium into the cytosol, and a *feed backward* coupling by including a current flux [54] in the HH-model equations which is driven by changes in the cytosolic Ca^{2+} completes bidirectionality of the system.

2.2. Calcium Dynamics and Membrane Transport Mechanisms. In previous work a three-dimensional model for intracellular Ca^{2+} dynamics was derived for the subcellular level [11, 12, 81]. These models, however, were derived to incorporate the detailed three-dimensional architecture of organelles and the cellular plasma membrane and did not include mechanisms of rapid endoplasmic refilling nor Alzheimer-relevant processes. Here, we provide the membrane transport mechanisms and a dimension-reduced one-dimensional model of the original 3D model by assuming local rotation symmetry and uniformly distributed transport mechanisms. The dimension-reduced diffusion-reaction system reads (see supplemental material SM1 for a derivation):

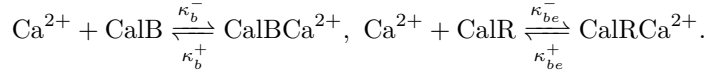
$$(2.2) \quad \frac{\partial c_c}{\partial t} = \frac{1}{(R^2 - r^2)} \frac{\partial}{\partial x} \left((R^2 - r^2) D_c \frac{\partial c_c}{\partial x} \right) + (k_b^- (b^{\text{tot}} - b) - k_b^+ b c_c) \\ + \frac{2r}{(R^2 - r^2)} J_{ERM} + \frac{2R}{(R^2 - r^2)} J_{PM}, \quad \text{in } \Omega_C$$

$$(2.3) \quad \frac{\partial c_e}{\partial t} = \frac{1}{r^2} \frac{\partial}{\partial x} \left(r^2 D_c \frac{\partial c_e}{\partial x} \right) + (k_{be}^- (b_e^{\text{tot}} - b_e) - k_{be}^+ b_e c_e) \\ - \frac{2}{r} J_{ERM} + \frac{2}{r} J_{SOC}, \quad \text{in } \Omega_{ER}$$

$$(2.4) \quad \frac{\partial b}{\partial t} = \frac{1}{(R^2 - r^2)} \frac{\partial}{\partial x} \left((R^2 - r^2) D_b \frac{\partial b}{\partial x} \right) + (k_b^- (b^{\text{tot}} - b) - k_b^+ b c_c), \quad \text{in } \Omega_C$$

$$(2.5) \quad \frac{\partial b_e}{\partial t} = \frac{1}{r^2} \frac{\partial}{\partial x} \left(r^2 D_{be} \frac{\partial b_e}{\partial x} \right) + (k_{be}^- (b_e^{\text{tot}} - b_e) - k_{be}^+ b_e c_e) \quad \text{in } \Omega_{ER}$$

Here R is the dendritic radius, r the endoplasmic radius (both are functions of x), k_s^p are rate functions controlling chemical reactions, b_s^{tot} the total buffer concentrations in cytoplasm and ER, and D_s are diffusion coefficients. These equations are defined in cytosolic (Ω_C) and ER domains (Ω_{ER}). Equation ?? models the diffusion-reaction of cytosolic calcium, where c_c is the cytosolic Ca^{2+} concentration and equation ?? models the diffusion-reaction of ER calcium where c_e is the endoplasmic Ca^{2+} concentration. Equations ?? and ?? model the diffusion-reaction of cytosolic Calbindin and Calreticulin, where b and b_e are Calbindin and Calreticulin concentrations, respectively. Both molecules buffer calcium, based on the reaction equations



The reactions are included in ?? and ??, as well as in ?? and ??, respectively. Equations ??, ?? both contain flux terms corresponding to the Ca^{2+} influx/efflux due to different membrane transport mechanisms (see below). The membrane transport mechanisms are realized by including fluxes J_{PM} and J_{ER} . The term J_{PM} is the net Ca^{2+} ion flux across the plasma membrane, and J_{ERM} is the net Ca^{2+} ion flux across the ER membrane. The two fluxes are further compartmentalized by the mechanisms that are transporting Ca^{2+} across the membranes, that is

$$(2.6) \quad J_{PM} = -J_P - J_N + J_{VDC} + J_{SYN} + J_{l,p}, \quad \text{on } \Gamma_{PM}$$

$$(2.7) \quad J_{ERM} = J_{RyR} - J_S + J_{SOC} + J_{l,e} \quad \text{on } \Gamma_{ERM}.$$

The flux terms for the plasma membrane (Γ_{PM}) are as follows: J_P is the Ca^{2+} flux from plasma membrane Ca^{2+} -ATPase pumps (PMCA), J_N is the flux due to $\text{Na}^+/\text{Ca}^{2+}$ exchangers (NCX), J_{VDC} is the flux from VDCCs, J_{SYN} is the calcium influx through the post-synaptic density (PSD), and $J_{l,p}$ is the leak calcium flux across the plasma membrane.

Fig. 1A provides an overview of various components and their operating domains modeled in this study in an unbranched neurite. Fig. 1B,C provides a visualization of the full neuron geometry used in this study in 2D and 3D view.

The flux terms for the ER are as follows: J_{SOC} is the flux from store-operated calcium channels [68, 32], J_{RyR} is the flux from ryanodine receptors [12, 11, 53, 80, 81], J_S is the flux from sarco/endoplasmic reticulum Ca^{2+} -ATPase pumps [88], and $J_{l,e}$ is the leak calcium flux. Each flux term is of the form

$$(2.8) \quad J_X = \rho_X \cdot p_X^o \cdot I_X,$$

where ρ_X is the density of the transport mechanism per unit area, p_X^o is the open state probability of a single channel which is unitless, and I_X is the Ca^{2+} current in units of concentration per time. Homogeneous distributions of all exchange mechanisms were assumed, as experimental data on precise numbers of spatial distribution of these mechanisms are not readily available. In the following paragraphs we describe each of the flux functions used in our study, along with references to the published models and available experimental data.

PMCA Pumps. For the PMCA pumps we used the model found in [34, 33], where the plasma membrane Ca^{2+} current is modeled as a second-order Hill equation

$$J_P(c_c) = \rho_P \cdot \frac{I_P c_c^2}{K_P^2 + c_c^2},$$

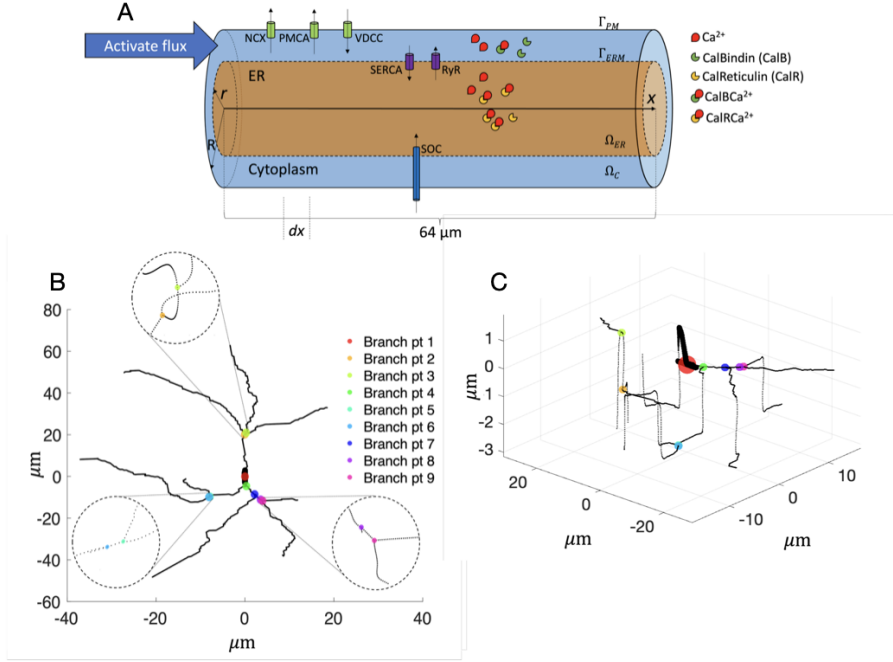


FIG. 1. (A) Schematic of unbranched neurite with model components and simulation domains. The neurite is $64 \mu\text{m}$ in length with dendrite radius ($R = 0.4 \mu\text{m}$) and ER radius ($r = 0.15 \mu\text{m}$). The two domains are ER (Ω_{ER}) and cytoplasm (Ω_C) with Γ_{PM} and Γ_{ERM} being plasma membrane (PM) and ER membrane (ERM) boundary. Ca^{2+} is present in both cytoplasm and ER domains while Calbindin and Calreticulin are present only in cytoplasm and ER, respectively. The Ca^{2+} buffering reaction and diffusion takes places in Ω_{ER} and Ω_C domains. NCX, PMCA and VDCC transports Ca^{2+} across PM. SERCA and RyR transports Ca^{2+} across ERM. For our simulation settings, SOC transports Ca^{2+} from extracellular space to ER. Activation flux enters through cytoplasmic domain on the left hand side. (B) Full neuron geometry used in the presented simulations with 9 branching points. (C) 3D view of the geometry with branching points. The thick region at the branching point 1 (red point) is the soma of the neuron

where ρ_P is the density of PMCA pumps on the plasma membrane, I_P is the single channel Ca^{2+} current, c_c is the cytosolic Ca^{2+} concentration, and K_P is the measure of Ca^{2+} affinity. Values for the constants in this equation were borrowed from [11, 12].

NCX Exchangers. The NCX exchange mechanism moves Ca^{2+} from the cytosol to the extracellular region of the neuron. The NCX transport mechanism is responsible for keeping the cytosolic calcium concentration low, and has low affinity to calcium, i.e. the NCX proteins do not bind closely to calcium ions. Therefore, in order for NCX pumps to be effective, they need to register high calcium concentrations. For the NCX exchange current we assume a fixed Na^+ concentration at the plasma membrane, utilizing a first-order Hill equation from [34, 33]:

$$J_N(c_c) = \rho_N \cdot \frac{I_N c_c}{K_N + c_c},$$

where ρ_N is the density of NCX exchangers on the plasma membrane, I_N is the single channel Ca^{2+} current, c_c is the cytosolic Ca^{2+} concentration, and K_N is the measure of Ca^{2+} affinity for NCX exchangers. All values for the constants in this equation

were borrowed from [11, 12].

VDCCs. For the voltage dependent calcium channels, we follow the Borg-Graham model found in [37, 8] and the Ca^{2+} current is given by

$$J_{VDC}(V, c_c, t) = G(V, t)F(V, \Delta[\text{Ca}^{2+}]),$$

where $G(V, t) \in [0, 1]$ is the gating function which depends on the membrane voltage V at time t , and $F(\cdot, \cdot)$ is the flux function. Both of these functions depend on the voltage at the channel at time t and we assume a prescribed density on the plasma membrane. For the flux function $F(\cdot, \cdot)$, the quantity $\Delta[\text{Ca}^{2+}]$ is the difference between the cytoplasmic and extracellular (c_o) ion concentration

$$\Delta[\text{Ca}^{2+}] = c_c - c_o$$

and the flux function is computed using the Goldman-Hodgkin-Katz equation

$$F(V, \Delta[\text{Ca}^{2+}]) = \bar{p}_{\text{Ca}^{2+}} \frac{Vz^2F^2}{RT} \cdot \frac{c_c - c_o \exp(-zFV/RT)}{1 - \exp(-zFV/RT)},$$

where R is the universal gas constant, F is Faraday's constant, T is temperature in Kelvin, $\bar{p}_{\text{Ca}^{2+}}$ is the permeability of Ca^{2+} ions through the channels, and z is the valence of a Ca^{2+} ion. The gating function is expressed as

$$G(V, t) = \prod_i x_i^{n_i}(V, t),$$

where $x_i^{n_i}$ is the open probability of the Ca^{2+} gating particle and n_i is the number of particles. The open probability is described by the ODE

$$\frac{dx_i}{dt} = \frac{x_\infty(V) - x_i}{\tau_{x_i}(V)},$$

where x_∞ is the steady-state value of the probability, and τ_{x_i} is the time constant for the particular particle. Each particle has an associated kinetic function for the open and closed states, in this case it is $\alpha_i(V)$ and $\beta_i(V)$, and from this we compute the time constant

$$\tau_{x_i} = \frac{1}{\alpha'_i(V) + \beta'_i(V)} + \tau_0.$$

As an example, the gating function $G(\cdot)$ for N-Type VDCCs is described by

$$G(V, t) = k(V, t)l^2(V, t),$$

where the gating functions $k(\cdot)$ and $l(\cdot)$ satisfy the ODEs

$$\frac{\partial k}{\partial t} = \frac{k_\infty - k}{\tau_k} \quad \text{and} \quad \frac{\partial l}{\partial t} = \frac{l_\infty - l}{\tau_l},$$

where

$$k_\infty = \frac{\alpha_k(V)}{\alpha_k(V) + \beta_k(V)}; \quad l_\infty = \frac{\alpha_l(V)}{\alpha_l(V) + \beta_l(V)},$$

and

$$\tau_k = \frac{1}{\alpha_k + \beta_k} + \tau_{k,0}; \quad \tau_l = \frac{1}{\alpha_l + \beta_l} + \tau_{l,0}.$$

The rate functions are given by

$$\begin{aligned}\alpha_k(V) &= K_k \exp\left(\frac{z_k \gamma_k (V - V_{1/2,k}) F}{RT}\right) \\ \beta_k(V) &= K_k \exp\left(\frac{-z_k (1 - \gamma_k) (V - V_{1/2,k}) F}{RT}\right) \\ \alpha_l(V) &= K_l \exp\left(\frac{z_l \gamma_l (V - V_{1/2,l}) F}{RT}\right) \\ \beta_l(V) &= K_l \exp\left(\frac{-z_l (1 - \gamma_l) (V - V_{1/2,l}) F}{RT}\right)\end{aligned}$$

and the values and descriptions of the constants used in the above equations can be found in [37].

Additionally, we also utilize parameters found in [8, 37] that differentiate between N-type and T-type channels which are high-voltage-activate (HVA) and low-voltage-activated (LVA), respectively.

For the presented research we compared the cytoplasmic Ca^{2+} response for a model with and without VDCC coupling. For VDCC coupling, we tested N-type and T-type channels, using parameters found in [8, 37]. We noticed that the coupled VDCC models have different cytoplasmic Ca^{2+} responses compared to the uncoupled VDCC model (see supplemental Fig. SM3).

RyR Channels. The model equations for ryanodine receptor (RyR) channels are of the form

$$J_{\text{RyR}}(c_c, c_e) = \rho_{\text{RyR}} \cdot p_{\text{RyR}}^o \cdot I_{\text{RyR}}(c_c, c_e),$$

where ρ_{RyR} is the density, p_{RyR}^o is the open state probability, and $I_{\text{RyR}}(c_c, c_e)$ is the Ca^{2+} current through a single RyR channel. From [12, 11, 53, 80, 81] we describe the current by

$$I_{\text{RyR}}(c_c, c_e) = I_{\text{RyR}}^{\text{ref}} \cdot \frac{c_e - c_c}{c_e^{\text{ref}}},$$

where the reference current $I_{\text{RyR}}^{\text{ref}}$ is taken from data found in [96]. The open probability for RyR channels is taken from [12, 11, 53], which is calculated by summing the two open states o_1 and o_2 , that is $p_{\text{RyR}}^o = o_1 + o_2$. The values of the open states are governed by a system of ordinary differential equations

$$\begin{aligned}o_1 &= 1 - c_1 - o_2 - c_2, \\ \frac{\partial c_1}{\partial t} &= k_a^- o_1 - k_a^+ c_c^4 c_1, \\ \frac{\partial o_2}{\partial t} &= k_b^+ c_c^3 o_1 - k_b^- o_2, \\ \frac{\partial c_2}{\partial t} &= k_c^+ o_1 - k_c^- c_2,\end{aligned}$$

where the kinetic values k_a^\pm , k_b^\pm , and k_c^\pm are given in Table SM1. This system of ODEs is solved independently at every point on the 1D domain of the ER.

SERCA Pumps. For the current flux from sarco/endoplasmic reticulum Ca^{2+} -ATPase (SERCA) pumps we use a model from [88] given by

$$J_S(c_c, c_e) = \rho_S \cdot \frac{I_S c_c}{(K_S + c_c) c_e},$$

where ρ_S is the density of SERCA pumps on the ER membrane, I_S is the maximum Ca^{2+} current, and K_S is the affinity of Ca^{2+} . This model was chosen because it includes the dependence of Ca^{2+} current on the cytosolic Ca^{2+} concentration and ER saturation. The values of the constants are given in Table SM1.

SOC Channels. Store-Operated Calcium (SOC) channels serve an important function in ER refilling [72, 77]. While many models have been recommended to model the SOC flux [68, 32, 29, 31] we followed the format of (2.8) with a current adapted from [68, 32]. The model we implemented considers a Ca^{2+} SOC-flux directly from the extracellular space into the ER. The model equation is as follows

$$J_{SOC}(c_o, c_e) = \rho_{SOC} \cdot p_{SOC}^o \cdot I_{SOC}(c_o, c_e),$$

where

$$(2.9) \quad p_{SOC}^o = \begin{cases} 1, & \text{if } c_e \leq c_{cutoff}, \\ (e^{c_{e,eq} - c_e} - 1)/10 & \text{otherwise,} \end{cases}$$

$$I_{SOC}(c_o, c_e) = \frac{I_{SOC}^{ref}}{F \cdot z} \cdot \log \left(\frac{10 \cdot c_o}{c_e} \right),$$

where $c_{e,eq}$ is the equilibrium ER Ca^{2+} concentration ($250 \mu\text{M}$), ρ_{SOC} is the density, p_{SOC}^o is the open state probability, and $I_{SOC}(c_o, c_e)$ is the Ca^{2+} current through a single SOC channel. The model parameters and values are given in Table SM1. We model the open probability p_{SOC}^o as a smooth switch between ‘on’ and ‘off’ state. The value c_{cutoff} (see Fig. SM1c.) is calculated such that it satisfies

$$1 = \frac{e^{c_{e,eq} - c_{cutoff}} - 1}{10},$$

$$c_{cutoff} = 247.602 \mu\text{M}.$$

A β pores. The leakage current associated with leaky synapses due to amyloid β (A β) pores is modeled from [19, 60] as follows:

$$J_{A\beta} = L_i k_\beta a^m,$$

where k_β is rate constant, a is the amyloid concentration, m is a cooperativity coefficient and L_i is the number of leaky synapses at node i . For an unbranched neurite $L_i = 1$, meaning only one leakage term is associated at a given node. The flux $J_{A\beta}$ is added to the plasma membrane leakage flux (see Sec. 2.4). The values of the constants are given in Table SM1.

Plasma and ER Membrane Leak. The ER membrane and plasma membrane both have a leakage flux that needs to be accounted for and incorporated with described transport mechanisms. The leakage fluxes are calculated to ensure a zero membrane net flux at equilibrium for all simulated ions and agents. Leakage flux densities are modeled by

$$J_{l,e}(c_c, c_e) = v_{l,e} \cdot (c_e - c_c),$$

$$J_{l,p}(c_c) = v_{l,p} \cdot (c_o - c_c),$$

where c_o is the extracellular Ca^{2+} concentration, which is assumed constant. This is a reasonable assumption as it has been shown that in the synaptic cleft, a very isolated region of extracellular domain, the recovery to baseline happens within 2 ms [30]. This corresponds to a threshold frequency of 500 Hz whereas our simulation frequencies are in the range of 1-10 Hz. All values for the constants in this equation were borrowed from [11, 12]. During each run, velocities are calculated by following set of equations

$$\begin{aligned} v_{l,e} &= (J_S - J_{RyR}) / (c_{e,eq} - c_{c,eq}), \\ v_{l,p} &= (J_P + J_N - J_{VDC}) / (c_o - c_{c,eq}), \end{aligned}$$

where $c_{c,eq}$ and $c_{e,eq}$ are cytosolic and ER Ca^{2+} concentrations at equilibrium.

Synaptic Influx. We approximate the PSD calcium influx by a linear decreasing function [12, 81]:

$$J_{SYN} = j_{rls} \cdot \left(1 - \frac{t - t_0}{\tau_{rls}}\right) \lambda_{t_0}(t),$$

where j_{rls} is the specific current density and τ_{rls} is the associated time constant. This function was chosen based on prior work from [12, 81] and from Ca^{2+} profiles found in [58]. The function $\lambda_{t_0}(t)$ is given by:

$$\lambda_{t_0}(t) = \begin{cases} 1, & t \in [t_0, t_0 + \tau_{rls}] \\ 0, & \text{otherwise.} \end{cases}$$

For our experiments we used this influx current in ?? at randomly chosen locations on the neuron geometry, at random start times in a time window $t_0 \in [t_{start} - t_{end}]$, and with random specific current densities. Therefore, at a location x_{SYN} , the flux J_{SYN} with H healthy synaptic sources becomes

$$(2.10) \quad J_{SYN} = \sum_{k=1}^H j_{rls,k} \cdot \left(1 - \frac{t - t_{0,k}}{\tau_{rls}}\right) \lambda_{t_{0,k}}(t),$$

where $t_{0,k} \in [t_{start} - t_{end}]$ and each $t_{0,k}$ is chosen randomly in the range. Additionally, the value of τ_{rls} is fixed and is given in Table SM1.

Summary of the Ca^{2+} model. With the implementation of all Ca^{2+} model dynamics described above, we show the typical concentration profiles on an unbranched neurite in Fig. 2. One can observe individual Ca^{2+} spikes in the cytosol (Fig. 2A) interacting with the buffer calbindin. This results in the formation of a CalBCa^{2+} complex causing a reduction of free CalB (Fig. 2B). The cytosolic spike results from Ca^{2+} release from the ER which causes a reduction of c_e (Fig. 2C). This in turn increases the free Calreticulin concentration by releasing bound Ca^{2+} in ER (Fig. 2D). These dynamics create stable calcium-induced calcium (CICR) waves (Fig. 2E) that are able to travel along neurites over long distances. Repetitive activation of CICR waves requires the ER to refill. For this purpose, four separate simulations on an unbranched neurite were performed with SERCA flux only, SERCA flux and CalR, SERCA and SOC flux, and all three combined. The ER refilling profile for the four cases is seen in Fig. 2F. The SERCA-only case increases ER Ca^{2+} concentration rapidly in the beginning by moving Ca^{2+} ions from the cytoplasm to the ER, but the flux intensity decreases when the cytoplasmic Ca^{2+} concentration gradually reaches equilibrium resulting in a plateau of ER Ca^{2+} below equilibrium. Addition of SOC fluxes results in

rapid increase in ER Ca^{2+} concentration towards equilibrium but leads to unprovoked bursts of Ca^{2+} release into the cytoplasm. Combining SERCA flux, SOC flux and ER buffer (CalR) allows rapid and stable increase in ER Ca^{2+} concentration. Removing SOC results in the slowest ER concentration increase, therefore establishing the importance of SOC in refilling of ER. Fig. 2G Top panel demonstrates evolution of Ca^{2+} wave over the full neuron geometry. The color indicates the cytoplasmic Ca^{2+} concentration. At $t = 20.1 \text{ ms}$, the neuron is at the equilibrium state. It is stimulated at $t = 23.1 \text{ ms}$ at various synapses and Ca^{2+} wave travels through the neuron ($t = 25.1 \text{ ms}$ and $t = 40.1 \text{ ms}$). At $t = 70.1 \text{ ms}$, the cytoplasmic Ca^{2+} concentration starts to fall down to equilibrium state. The cytoplasmic Ca^{2+} response at soma over time is plotted in Fig. 2G Bottom panel. We also provide video demonstrations (see supplemental materials) of the full neuron geometry stimulated at 1 and 5 Hz frequency. It is accompanied with a cytoplasmic Ca^{2+} profile at one of the branch points.

In our study, we find that the Ca^{2+} wave features are comparable to ones observed experimentally. For instance, on the unbranched neurite geometry, Ca^{2+} wave amplitudes are around $3\text{--}4 \text{ }\mu\text{M}$ which is comparable to $1\text{--}10 \text{ }\mu\text{M}$ wave amplitudes observed in the literature [85, 59, 70, 6]. Ca^{2+} wave speeds in simulations are around $500 \text{ }\mu\text{m/s}$ on the same unbranched neurite, while observed wave velocities in neurons in the literature range between $60\text{--}200 \text{ }\mu\text{m/s}$ [48, 16, 82]. We note that these quantities are affected by the size and shape of neurons [12, 9]. Confirming these values generally is hard as it has, e.g., been shown that cellular Ca^{2+} responses differ when activating the same synapses but in different order [10]. We used a stimulation frequency of 1Hz and 5Hz to cover the frequency range known to be relevant for learning and plasticity [27, 28, 56]. Furthermore, the filtering effect seen in our simulations is also observed experimentally [10].

2.3. Modeling Electrical Dynamics. Electrical neuronal activity was modeled with the classical Hodgkin-Huxley equations [37, 44, 42, 41, 43, 45], including explicit terms for sodium, potassium, and calcium ions:

$$(2.11) \quad C \frac{\partial V}{\partial t} = \frac{1}{R_{ax}} \frac{\partial V}{\partial x} \left(a(x) \frac{\partial V}{\partial x} \right) + I_{HH}(V, n, m, h) + I_{CaF}(V, c_c, x, y).$$

Here, V is the membrane potential, C the membrane capacitance, a the neurite radius, R_{ax} the axial resistance of the neurite, $I_{HH}(\cdot)$ the ionic current contribution from sodium, potassium, and leak, and $I_{CaF}(\cdot)$ is the fast Ca^{2+} current contribution. The state variables for the potassium and sodium channels are given by n for potassium, and m, h for sodium. For the fast Ca^{2+} current the variables x, y denote the state variables. The ionic current contribution $I_{HH}(\cdot)$ is given below for completion:

$$I_{HH}(V, n, m, h) = \bar{g}_K n^4 (V_K - V) + \bar{g}_{Na} m^3 h (V_{Na} - V) + \bar{g}_l (V_l - V).$$

Here, n , m , and h are the state variables for potassium (n) and sodium (m, h). The last term is the leakage term for ions not directly accounted for. The variables \bar{g}_K and \bar{g}_{Na} correspond to the maximum conductance for the potassium and sodium ion channels, respectively. The variable \bar{g}_l is the leak conductance. The variables V_K , V_{Na} , and V_l are the potassium, sodium, and leak reversal potentials, respectively.

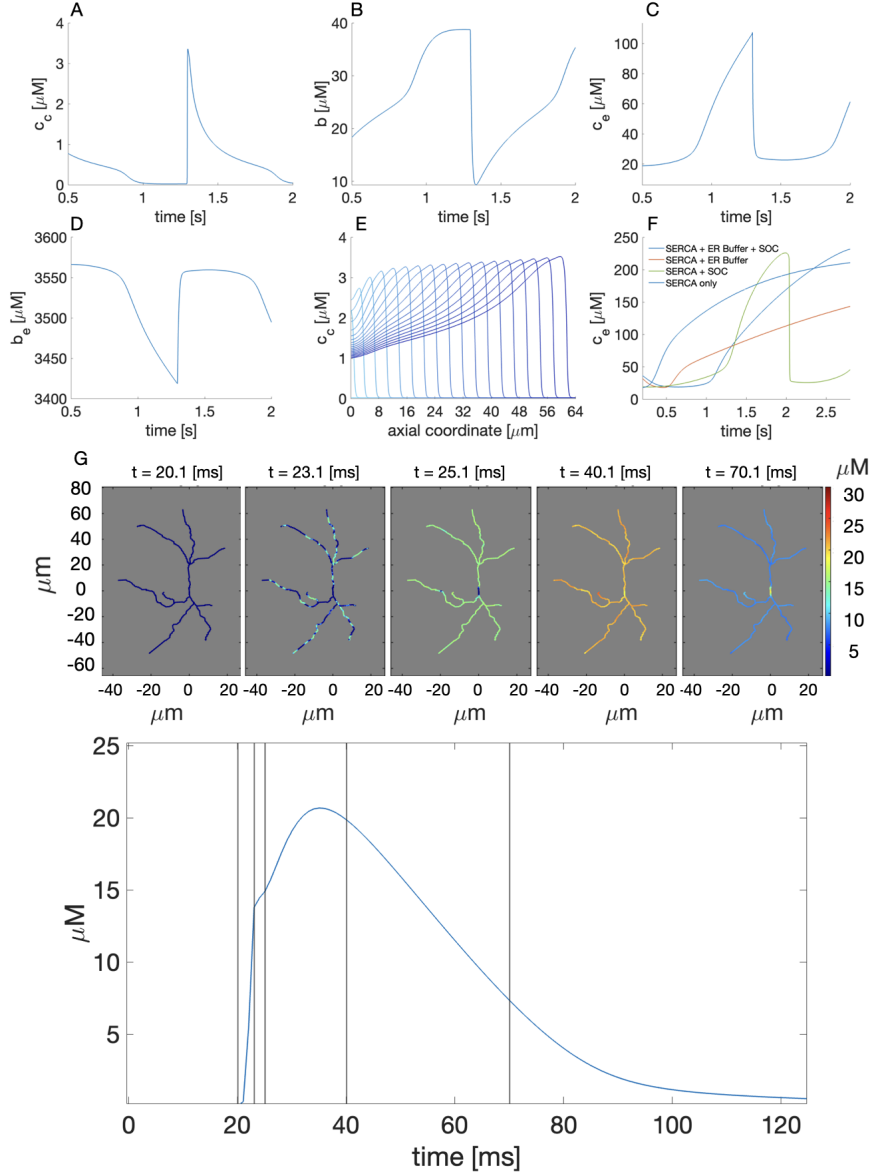


FIG. 2. Dynamics in an unbranched neurite. (A-D) Concentration profiles for all modeled species measured at the soma. As the calcium wave reaches the soma, there is a spike in cytosolic Ca^{2+} concentration (A). This spike corresponds to a reduction in free CalB (B) as a result of fast buffering action of CalB on excess calcium in the cytoplasm rapidly forming CalBCa^{2+} complex. The calcium-induced calcium response causes instant release of ER Ca^{2+} (c_e) into cytosol seen as massive dip in c_e (C). The decrease in c_e triggers release of Ca^{2+} bound to CalR (b_e) thereby increasing free CalR concentration in ER (D), (E) Stable calcium wave propagating through neurite cytoplasm translates and carries electrical signal from synapses to nucleus. The wave travels at the speed of approximately $0.5 \mu\text{m/ms}$. Each line represents 7.5 ms time difference from each other, (F) ER refilling is mediated by SERCA channels along with Store operated channels. Additionally, huge amount of Ca^{2+} is stored as buffered Ca^{2+} by CalR which is released instantly as ER discharges Ca^{2+} into cytoplasm. Combined, these three mechanisms ensure that ER holds enough Ca^{2+} to release upon repeated activations. Neuronal response to stimulation of 1000 synaptic junctions. (G) **Top:** The evolution of calcium wave over the neuron. The color represents cytosolic calcium concentration. Initially, c_c is low at 50 nM . The plot at $t = 23.1 \text{ ms}$ demonstrates triggering/stimulation of synapses at various locations of neuronal dendrites causing initiation of many calcium waves. These calcium waves travel throughout the body of neuron leading to increase in c_c (at $t = 25.1 \text{ ms}$ and $t = 40.1 \text{ ms}$). Once the wave passes, the c_c begins to fall to equilibrium state ($t = 70.1 \text{ ms}$). **Bottom:** Cytosolic calcium concentration at the soma over the simulation period. Each vertical line corresponds to the snapshot time in top panel.

Equation ?? couples to the state ODEs, which we provide below:

$$\begin{aligned}\frac{dn}{dt} &= \alpha_n(V)(1 - n) - \beta_n(V)n, \\ \frac{dm}{dt} &= \alpha_m(V)(1 - m) - \beta_m(V)m, \\ \frac{dh}{dt} &= \alpha_h(V)(1 - h) - \beta_h(V)h,\end{aligned}$$

where the functions $\alpha_i(\cdot)$ and $\beta_i(\cdot)$, with $i \in \{n, m, h\}$, are rate functions. Below we provide the rate functions for completion, borrowed from [75, 81]:

$$\begin{aligned}\alpha_n(V) &= \frac{-0.32(V - 15)}{\exp\left(\frac{15 - V}{5}\right) - 1}, & \beta_n(V) &= 0.5 \exp\left(\frac{10 - V}{40}\right), \\ \alpha_m(V) &= \frac{-0.32(V - 13)}{\exp\left(\frac{13 - V}{4}\right) - 1}, & \beta_m(V) &= \frac{0.28(V - 40)}{\exp\left(\frac{V - 40}{5}\right) - 1}, \\ \alpha_h(V) &= 0.128 \exp\left(\frac{17 - V}{18}\right), & \beta_h(V) &= \frac{4}{\exp\left(\frac{40 - V}{5}\right) + 1}.\end{aligned}$$

For the fast Ca^{2+} current contribution we borrow equations from [76, 54], where

$$I_{CaF}(V, c_c, \sigma, \rho) = \bar{g}_{Ca} \sigma \rho (V_{Ca} - V),$$

and V_{Ca} is the Ca^{2+} -dependent reversal potential, given by the Nernst equation

$$V_{Ca} = 12.5 \cdot \log\left(\frac{c_o}{c_c}\right).$$

The variables σ and ρ have corresponding equations, where

$$\frac{d\sigma}{dt} = \frac{\sigma_\infty - \sigma}{\tau_\sigma}$$

is the governing ODE with

$$\tau_\sigma = \frac{7.8}{\exp((V + 6)/16) + \exp(-(V + 6)/16)}, \quad \sigma_\infty = \frac{1}{1 + \exp(-(V - 3)/8)}.$$

The variable ρ is computed by

$$\rho(c_c) = \frac{K}{K + c_c},$$

with K fixed (see Table SM2). Note, the term $I_{CaF}(\cdot)$ couples the calcium model to the electrical model.

2.4. Modeling synapses. In Sec. 3 we make use of a test geometry, which is an unbranched neurite, and an anatomical neuron reconstruction. For the unbranched neurite, we place one synapse at the first point (left most point) of the geometry such that there is only one synaptic Ca^{2+} source.

For the full neuron geometry, let S be the total number of synapses that are distributed across the neuron. This will include healthy and leaky synapses, $S =$

$H + L$, where H is the number of healthy and active synapses and L is the number of leaky synapses. The neuronal geometry is represented as a discrete set of nodes with a connectivity graph and neurite diameters attached to each node, where the neuron's graph G contains N nodes. We distribute the number of synapses S across the N nodes. For example, at node x_i there are H_i, L_i healthy and leaky synapses, respectively. It is possible for some nodes not to contain synapses ($H_i = L_i = 0$) which may occur if $N \gg S$. Therefore, $S = \sum_{i=1}^N H_i + L_i$ and synaptic influx is modelled by eq. ?? .

In order to model pure synapse loss we do not include leaky terms associated with amyloid β and only modify the value of H_i (see Sec. 3. Synaptic influx at only healthy synapses (H) are modeled as leaky synapses (L) are modeled by deactivating leaky synapses. For an unbranched neurite the same applies with $H_1 = 1$ and there is no synapse loss.

The leakage flux associated with amyloid β is added to $J_{l,p}(c_c)$ if a synapse is set as leaky. This mimics the constant leak into the cytoplasm at equilibrium by amyloid β clustering (see Sec. 3.3). The flux $J_{l,p}(c_c)$ then becomes

$$J_{l,p}(c_c) = v_{l,p} \cdot (c_o - c_c) + \delta \cdot J_{A\beta},$$

where $\delta = 1$ if the node contains leaky synapses and $\delta = 0$ otherwise. In the unbranched neurite test geometry, while simulating leakiness, every third node is set as leaky. In order to model synapse loss with leakage in full neuron geometry, δ for synapses in L is set to 1. At the leakage site, $J_{A\beta}$ is continuously added throughout the simulation to mimic leakage occurring in biologically realistic scenarios.

2.5. Neuron reconstructions. Simulations were carried out on two geometries, (1) an unbranched, symmetric cable (see Fig. 1A), representing a dendrite with a length of $64 \mu m$, a dendrite diameter of $0.8 \mu m$ and ER diameter of $0.3 \mu m$ and (2) an anatomical reconstruction of an adult female mouse brain-stem neuron [7] borrowed from [NeuroMorpho.org](https://neuroMorpho.org) [3], with identification NM0_150605. While the simplified dendritic geometry was used for illustrating the fundamental dynamics that emerge from the coupled electro-calcium model in Sec. 2.2–2.4, the neuronal geometry was used to study the effects of changes in parameters affected by AD in a realistic setting.

Both geometries were processed to have a quasi-uniform edge length defined by Δx and therefore the number of nodes is given by $N = \lfloor \frac{l}{\Delta x} \rfloor + 1$, l being the total dendritic length. We then chose the edge length to be $\Delta x_m = 2^{-m+2} \mu m$ with $m = 0, 1, 2, \dots$. These mesh hierarchies were used to carry out a numerical convergence analysis (see Sec. 2.6). All geometries used in this study were saved in `.swc` format, which is one of the standard readable text file formats for saving the graph connectivity and spatial structures of neuroanatomical reconstructions [90]. In this format neuron morphologies are saved as a table which contains N rows corresponding to each node of the geometry, and each row contains the following information

ID	TYPE	X	Y	Z	RADIUS	PID
----	------	---	---	---	--------	-----

where ID is the node id number ranging from $[1, N]$. TYPE identifies the neuronal compartment, where e.g. the value 1 denotes the soma and 2 a dendrite (note, other identifiers exist). X, Y, Z are the spatial coordinates of the node, RADIUS is the radius of the neurite at the node, and PID is the parent id of the node. Note, that the set of $N - 1$ pairs (PID, ID) define the set of edges of the neuron graph, which defines the connectivity map of the geometry.

2.6. Numerical Methods. To solve the model equations presented in Sec. 2.2–2.4 on discrete geometries (see Sec. 2.5) we employed a semi-implicit time stepping

scheme with finite difference discretization of the spatial domain. Equations ??–?? , and ?? can each be expressed as

$$X_t = AX + BX$$

$$s_t = 0s + Fs.$$

where A is the discretization of the second order differential operator ∂_{xx} and B is the reaction function. For the Ca^{2+} equations B contains the current influx terms and any additional reaction terms, and for the Hodgkin-Huxley model equation ?? the B term would be the sum of the ion currents. Note, in the first equation $X = (c_c, c_e, b, b_e)$ while the second equation stands for the state variables used in the Hodgkin-Huxley model, i.e. $s = (n, m, h)$. The implicit-explicit time stepping method we implemented is the semi-implicit backward differentiation formula of second order (SBDF2) [83, 2, 81], which is given by the update rule

$$\frac{3}{2}X^{i+1} - 2X^i + \frac{1}{2}X^{i-1} = \Delta t AX^{i+1} + 2\Delta t BX^i - \Delta t BX^{i-1},$$

which yields

$$\left(I - \frac{2}{3}\Delta t A\right)X^{i+1} = \frac{4}{3}X^i + \frac{4}{3}\Delta t BX^i - \frac{1}{3}X^{i-1} - \frac{2}{3}\Delta t BX^{i-1}.$$

For the state variables a matrix of zeros is used for the right hand side and is written as

$$s^{i+1} = \frac{4}{3}s^i + \frac{4}{3}\Delta t Fs^i - \frac{1}{3}s^{i-1} - \frac{2}{3}\Delta t Fs^{i-1}.$$

For both equations, one needs to know the current state X^i, s^i and the prior state X^{i-1}, s^{i-1} to compute the next states.

For the spatial discretization, we consider the 1D nature of the geometry and apply finite differences [61] at every node of the geometry. As an example we consider a non-branched piece of dendrite with nodes x_{-1}, x_0 , and x_1 . Then the approximation to the second order differential operator at location x_0 , with diffusion coefficient D , is given by

$$D \frac{\partial^2 u_0}{\partial x^2} \approx \frac{D}{(\Delta x)^2} (u_{-1} - 2u_0 + u_1)$$

where u corresponds to the ion concentration variables, i.e. $c_c, c_e \dots$ etc. However, a neuron contains branching locations; therefore, we use a generalized form of the above approximation for a branch point x_i with neighbors indexed by $j \in \mathcal{N}$, where \mathcal{N} contains the indices of the nodes that are neighbors to node i . Additionally, we allow non-uniform edge lengths. The approximation to the second derivative at a branch point x_i is given by (see [9]):

$$D \frac{\partial^2 u_i}{\partial x^2} \approx \frac{2D}{\sum_{j \in \mathcal{N}} (\Delta x)_j} \left(\sum_{j \in \mathcal{N}} \frac{u_j}{(\Delta x)_j} - u_i \sum_{j \in \mathcal{N}} \frac{1}{(\Delta x)_j} \right),$$

where $(\Delta x)_j = \|x_i - x_j\|_2$, the Euclidean distance between the two nodes x_i and x_j . The derivation and example cases of the above approximation to the second order derivative can be also be found in [9, 81]. Convergence analysis was conducted with

varying levels of refinements $m = 1 - 5$. The refinement level is associated with time steps $\Delta t_m = 160, 80, 40, 20, 10 \text{ ms}$ and edge length $\Delta x_m = 2, 1, 0.5, 0.25, 0.125 \mu m$. The result of convergence analysis is available in Fig. SM1. Refinement level 1 and 2 were too coarse for convergence (not plotted). Refinement 3 – 5 show convergence and the selected refinement level was 5 ($\Delta x = 0.125 \mu m$ and $\Delta t = 10 \text{ ms}$) for all simulations presented in Sec. 3.

3. Biological Results. Using the model described in Sec. 2 we studied the effect of parameters that are known to change during AD. We designed a baseline “healthy” neuron by randomly distributing 1,000 synapses on the dendritic tree of a neuron selected from NeuroMorpho.org [3, 7]. Synapses were then activated randomly within a defined time window of 10 ms. We used a stimulation frequency of 1Hz and 5Hz to cover the frequency range known to be relevant for learning and plasticity [27, 28, 56] and studied the effect of different frequencies on somatic calcium responses (see Sec. 3.1). The baseline neuron simulations used the default parameters listed in Table SM1. To illustrate the fundamental calcium dynamics of the model in Sec. 2 and the influence of specific parameter variations on synapse to soma communication we also used a simple test geometry, an unbranched neurite with constant dendritic and ER radius.

In this study we focused on three major parameters: (1) synapse loss [91, 94, 21], (2) calcium leaks at deteriorated synapses [22, 23, 47, 63, 52, 78, 25, 26, 57], and (3) downregulation of the calcium buffer calbindin in the cytosol [46, 55, 17, 71]. Synapse loss is a well documented effect seen in neurodegeneration [91, 94, 21]. This was modeled by pure removal of synapses from the pool of active synapses (see Sec. 3.2) and then by additionally adding a Ca^{2+} leakage term at deteriorated, leaky, synapses (see Sec. 3.3). Lastly, we studied what effect a 25% downregulation of Calbindin has on Ca^{2+} signaling in diseased neurons (see Sec. 3.4).

3.1. Neuronal frequency filtering from synapse to soma. Before modifying any biophysical parameters, we were interested in analysing the effect of different synapse stimulation frequencies on calcium signaling along the dendrites to the soma. Using the simple test geometry we stimulated at one end of the unbranched neurite and measured at the mid point (considered the soma). In Fig. 3A we see that at the location of stimulation calcium signals recover the 1 Hz stimulus, as well as the 5 Hz stimulus, although calcium amplitudes at the higher frequency are reduced. Moving away from the activation site, the “simple” neuron can reliably recover the 1 Hz frequency, but filters the 5 Hz stimulus and produces a roughly 1 Hz response.

The reason for this frequency filtering effect appears to lie in the kinetics of the ryanodine receptors. For a stable wave response to occur, a strong RyR current is needed, which occurs when p_{RyR}^o increases rapidly. One p_{RyR}^o cycle takes approximately 1 second. During this time period, any synaptic event has reduced impact on p_{RyR}^o , which leads to an abortive wave.

This is illustrated in Fig. 3A-C. Fig. 3A demonstrates c_c response to a 5 and 10 Hz input frequency at the synapse of the unbranched neurite. The responses to these inputs are filtered to 1 Hz at the soma, i.e., at the center node of the neurite (Fig. 3B). Fig. 3C shows p_{RyR}^o at the soma. In both cases p_{RyR}^o cycle time is $\approx 1\text{s}$. This makes the site unresponsive to incoming signals until p_{RyR}^o reaches equilibrium, after which the neurite can respond again.

We were interested whether this frequency filtering effect carries over to an actual neuron and repeated the computational experiment using a reconstructed neuron, see Fig. 3D-I, on which we placed 1,000 synapses randomly and triggered these at a 1

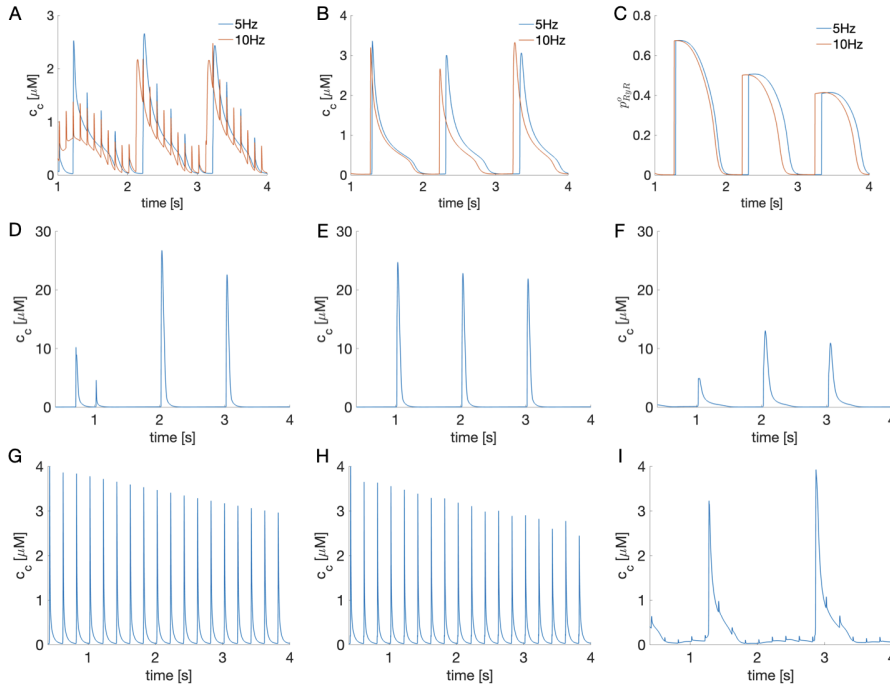


FIG. 3. Ca^{2+} response to varying levels of stimulation frequency at soma. (A-C) Response to 5 and 10 Hz stimulation on an unbranched neurite. (A) represents the Ca^{2+} profile of the stimulated synapse at 5 and 10 Hz. The input frequencies are filtered down to 1 Hz response at soma (B). This occurs due to the kinetics of RyR channels open state probability which takes almost 1 second to reduce down to zero after each wave event (C). (D-I) Response to varying levels of stimulation frequency in a full neuron at two branch points (points 2 and 8 in Fig. 1B.) and soma. (D-F) 1 Hz stimulus response at two branching points (D and E) and at the soma (F). While the 1 Hz stimulus frequency is detectable at all locations, most importantly at the soma, one can observe the dendritic tree resolving the high-frequency stimulus. (G-I) 5 Hz stimulus frequency travelling through the tree gets filtered to 3 Hz at the branch points (G and H) which further propagating towards and reaching the soma responds at a roughly 1 Hz frequency (I).

and 5 Hz frequency. We measured c_c response at branch points 2 and 8 and at the soma (see Fig. 1B,C). As seen in Fig. 3D, the neuron, independent of measurement site, is able to respond with a 1 Hz calcium signal that propagates towards the soma. However, when the stimulation frequency is increased to 5 Hz, we see that dendritic branches respond at roughly 3 Hz, which decays to 1 Hz responses at the soma (see Fig. 3G-I).

3.2. Effect of synapse loss on intracellular Ca^{2+} dynamics. Synapse loss is a well-documented part of AD and other neurodegenerative processes. Chemical synapses operate at multiple functional scales, e.g. transmitting electrical signals through release of neurotransmitters, but also by controlling Ca^{2+} entry into the cytosol at active post-synaptic sites. An influx of Ca^{2+} at the postsynaptic density can induce long-range Ca^{2+} signals, e.g. Ca^{2+} waves, by calcium-induced calcium-release (CICR) cascades at the endoplasmic membrane [99, 5]. Post-synaptic spine to dendrite communication, controlled by the intracellular organization and the stability of dendritic Ca^{2+} waves has been studied in the past [11, 12].

In healthy neurons, with an active and functioning synapse population, synapse

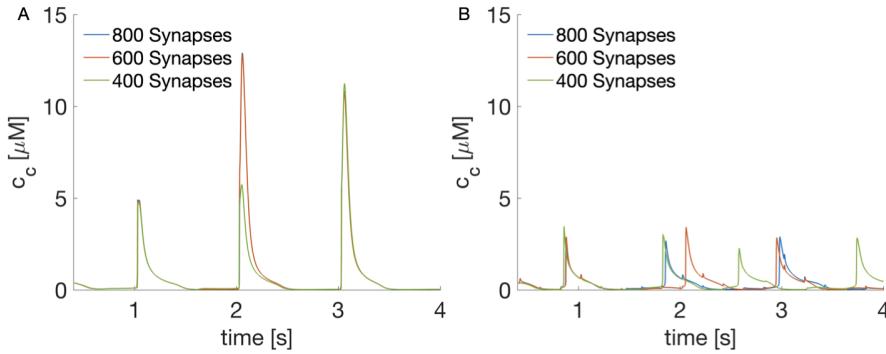


FIG. 4. Ca^{2+} response observed at soma at various levels of synapses loss. Originally, 800 active synapses (low level pathology) are considered from which 200 synapses were removed serially leaving 600 (medium level pathology) and 400 (high level pathology) active synapses. 1 Hz stimulus response (A) and 5 Hz stimulus response (B) were not significantly affected as a result of synapse loss.

to soma Ca^{2+} communication should be possible, as seen in Fig. 3. However, under conditions where the pool of active synapses is reduced, as in AD, a communication disruption between active synapses and the soma could potentially occur. This would have major implications for cell survival, since Ca^{2+} signals at the soma trigger biochemical cascades in the cell nucleus relevant for cell survival [5, 64, 69, 79]. There, amplitude, duration, and frequency of the Ca^{2+} signal regulates gene transcription responses [28, 62, 100].

We were therefore interested in studying the somatic Ca^{2+} response when iteratively removing synapses from the active pool. In Fig. 4 we show the somatic Ca^{2+} response for a low level pathology state (800 active synapses), medium level pathology state (600 active synapses), and high level pathology state (400 active synapses) at a 1Hz and 5Hz stimulation frequency. While there are observable fluctuations in the peak amplitudes of the signals and in the 5Hz case shifts in the frequency (and both could influence downstream biochemical cascades), Ca^{2+} signals are able to reach the soma even under significantly reduced active synapse scenarios. From the computational experiments it appears that neurons, with their intricate intracellular Ca^{2+} machinery, is well equipped to compensate significant synapse loss during neurodegeneration.

3.3. Leaky synapses disrupt synapse to nucleus pathway. Calcium entry into the cytoplasm from the extracellular space is controlled by calcium exchangers embedded in the plasma membrane [13, 33, 34]. In AD, it has been shown that the plasma membrane at deteriorated synaptic contacts can become leaky to Ca^{2+} [22, 23, 47, 63, 52, 78, 25, 26, 57] leading to Ca^{2+} accumulation in the cytoplasm. This disrupts the CICR release mechanism responsible for intracellular Ca^{2+} communication.

In addition to modeling synapse loss as described in Sec. 3.2, we made lost synapses leaky to Ca^{2+} by introducing a Ca^{2+} leakage term (see Sec. 2). We again incrementally decreased the pool of active synapses and made removed synapses leaky for Ca^{2+} . Fig. 5 shows the results for 800 active synapses (200 leaky synapses, low level pathology) to 400 active (600 leaky, high level pathology) at a 1 Hz and 5Hz stimulation frequency. With the decrease in active synapses, we initially observe similar results as described in Sec. 3.2. Peak Ca^{2+} amplitudes decrease with decrease of

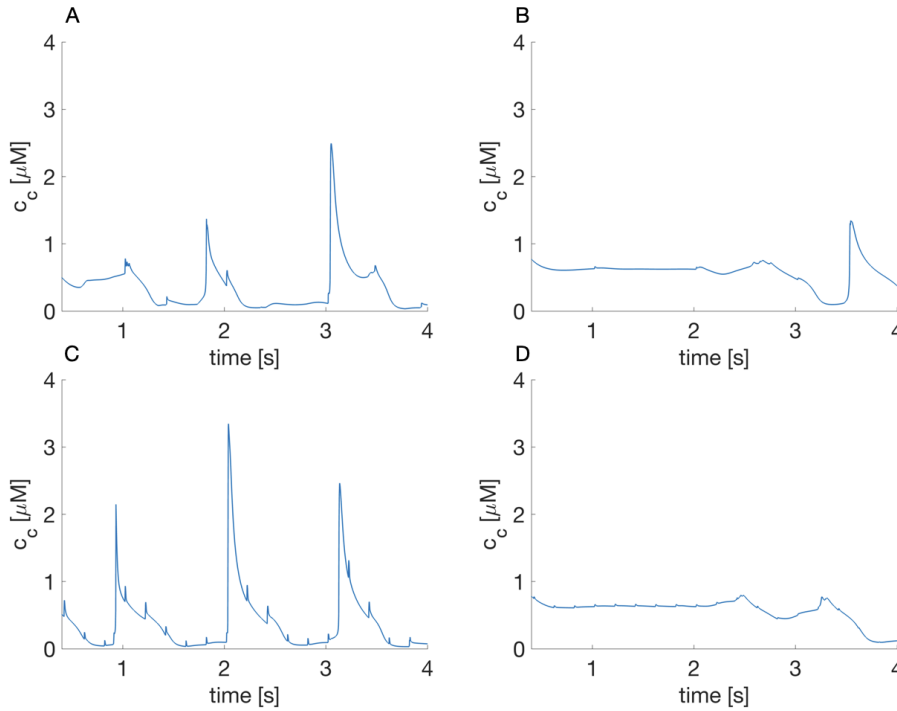


FIG. 5. Somatic Ca^{2+} response to synapse loss coupled with leakage caused due to amyloid β pores. The 1 Hz and 5 Hz stimulus response with 600 active synapses (medium level pathology, A and C respectively) disrupts signalling minimally. However, the 1 Hz and 5 Hz stimulus response with 400 active synapses (high level pathology, B and D respectively) causes significant disruptions to signalling. This is caused by accumulation of Ca^{2+} in cytoplasm thereby increasing equilibrium cytoplasmic Ca^{2+} levels.

active synapses and in the 5 Hz case a change in response frequency. However, when reaching roughly 400 active synapse sites (or 600 leaky, high level pathology), the somatic Ca^{2+} signal is entirely disrupted, i.e. no oscillating Ca^{2+} signal with distinct peak amplitudes are measurable. We describe this phenomenon as synapse to soma communication breakdown.

The accumulation of Ca^{2+} in the cytoplasm causes p_{RyR}^o to reach equilibrium state (i.e. zero) slowly. This maintains p_{RyR}^o at an elevated level and makes the ER unresponsive to a new activation flux. This significantly reduces strength of j_{RyR} which is the primary contributor to the spike in cytoplasmic Ca^{2+} needed for driving a Ca^{2+} wave/signal. Fig. SM2 demonstrates this phenomenon of accumulated cytosolic Ca^{2+} in an unbranched neurite with leaky synapses leading to elevated p_{RyR}^o levels over time in comparison to a neurite with non-leaky synapse states.

While neurons can apparently tolerate a significant degree of synapse loss without compromising synapse to soma communication, the introduction of Ca^{2+} leakiness at deteriorated synapses disrupts the intracellular Ca^{2+} signaling to the extent that somatic Ca^{2+} responses to low and high-frequency inputs are no longer measurable.

3.4. Downregulation of Ca^{2+} buffer Calbindin partially mitigates signal disruption from synapse loss. The last parameter we were interested in for this study was the intracellular Calbindin Ca^{2+} buffer concentration. The concentration

in healthy and AD neurons has been experimentally studied [46, 55, 17, 71] and a reduction in Calbindin concentration is documented in diseased neurons. We therefore reduced the basal Calbindin concentration by 25% (pathological concentration) and repeated the simulations of synapse loss with synaptic calcium leaks.

In Fig. 6 we show the results for healthy and pathological Calbindin concentrations at 5Hz stimulation frequency. First, we identified the synapse number at which, under normal Calbindin concentrations, we see the onset of synapse to soma communication breakdown (which occurs at around 460 active synapses). We then increased the number of active synapses to 470 and noticed that while under normal Calbindin concentrations there is only a small recovery towards a healthy somatic response, a pathological (decreased) Calbindin concentration allows the neuron to produce more robust Ca^{2+} signals at the soma.

Reduction in Calbindin has been observed in AD [55]. Cytoplasmic Calbindin plays an important role not only in Ca^{2+} buffering, but also in inhibiting apoptotic pathways. Reduction in Calbindin concentration has been shown to exacerbate AD pathologies and increased propensity of a neuron to enter apoptosis [55]. From this perspective the result that Ca^{2+} signalling is partially recovered by Calbindin reduction is exciting.

As dysregulation of Ca^{2+} signaling is an important feature of AD pathology, targeting this disruption pathway could be the basis for an effective treatment modality for AD [73]. It may be plausible that reduction of cytoplasmic Calbindin concentration could help neurons mitigate damage caused by elevated Ca^{2+} concentration in the cytoplasm.

Whether this improved cell signaling is helpful or detrimental to neurons needs further investigation.

4. Discussion. In this paper, we present a biophysical model of coupled calcium and electrical dynamics in neurons. The Ca^{2+} model is based on a previously developed three-dimensional model for ultrastructural simulations in neuronal sub-compartments [12, 11, 80]. In order to extend simulations to full cells for synapse to soma signaling, without making computations prohibitively costly, we assumed rotational symmetry of dendritic and endoplasmic segments at segment length scale of $10^{-1} \mu\text{m}$. The assumption of rotational symmetry allows us to derive a dimension-reduced version of the previous 3D model.

Since the biological focus of the presented work was to study Ca^{2+} signaling to the soma under healthy and neuropathological conditions, the model was developed to include relevant Ca^{2+} exchange mechanisms embedded in the plasma- and endoplasmic membranes. Voltage-dependent Ca^{2+} channels bidirectionally couple the Ca^{2+} and electrical model, which is based on the standard Hodgkin-Huxley formalism. To correctly capture endoplasmic Ca^{2+} exchange with the cytosol under repeated synaptic stimulation, we incorporated known ER refilling mechanisms that operate on different time scales: slow SERCA pump refilling, medium store operated Ca^{2+} channel refilling, and fast reaction of endoplasmic bound Ca^{2+} to free Ca^{2+} ions.

A reconstructed neuron from the NeuroMorpho.org [3, 7] database was used to carry out simulations of cellular Ca^{2+} dynamics. The resulting system of PDEs and ODEs were solved by spatial discretization of the computational domain and the PDEs using a finite difference approach. To address computational cost we chose SBDF2 as our time stepping scheme to treat stiff and non-stiff components separately and to avoid additional stage-computations per time step.

Using the developed biophysical model and computational framework we ad-

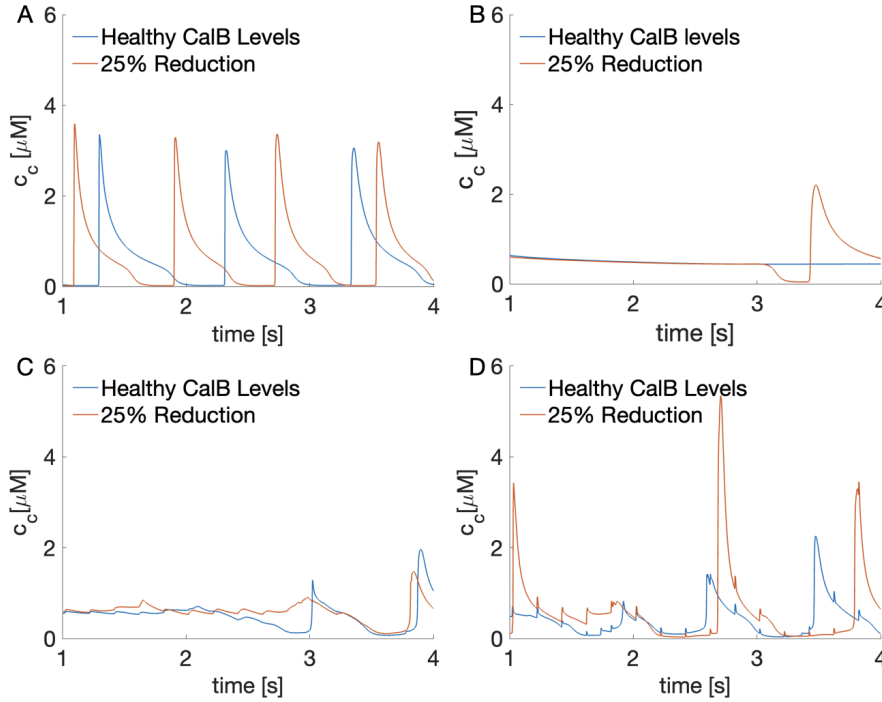


FIG. 6. Somatic Ca^{2+} response to downregulation of calbindin and synapse loss in an unbranched neurite (A-B) and full neuron geometry (C-D) at 5 Hz stimulation. (A) Baseline experiment with no leakage indicates increased frequency response to stimulus at 25% CalB reduction. (B) With leakage added, the wave responses at soma are delayed (compared to baseline) and only visible in pathological state in given simulation time. (C) The signalling is significantly disrupted in both healthy and pathological CalB concentration in full neuron geometry with 460 active synapses (540 leaky synapses). (D) Signalling is partially recovered at 470 active synapses (530 leaky synapses) when CalB is downregulated.

647 dressed the key question of how synapse to soma Ca^{2+} signals change due to pathology
 648 driven modulation of active synapse numbers, leakiness at deteriorated synapses and
 649 downregulation of Ca^{2+} buffering molecule Calbindin, all three modulations have
 650 been experimentally documented. This study revealed that pure synapse loss can be
 651 compensated well by neurons, although some changes in Ca^{2+} signal amplitudes, tim-
 652 ing, and frequency can be observed. If deteriorated synapses become leaky to Ca^{2+} ,
 653 which was modeled by an additional Ca^{2+} leakage term in the plasma membrane, and
 654 synapse loss becomes severe, synapse to soma communication breaks down, resulting
 655 in no controlled signals at the soma. This communication breakdown appears to be
 656 compensated to a certain extent by downregulation of Calbindin in the cytoplasm.

657 In forthcoming research we plan to integrate a numerical optimization strategy
 658 and use healthy neuron synapse to soma Ca^{2+} dynamics to formulate an objective
 659 function. Optimizing biophysical parameters in the biophysical model, such as channel
 660 densities, ER size, and reaction rates towards healthy Ca^{2+} dynamics from a patho-
 661 logical state could lead to new insight into how medical intervention may designed to
 662 counter synapse deterioration. Additionally, while reduction in Calbindin may help in
 663 recovering Ca^{2+} signaling, it has also been reported that it aggravates AD pathologies
 664 [55] due to its participation in many pathways including blocking apoptotic pathway.

This requires further investigation and factored in to create a more realistic model.

Acknowledgments. This research is supported by NIH grant R01EB034143. This research further includes calculations carried out on HPC resources supported in part by the National Science Foundation through major research instrumentation grant number 1625061 and by the US Army Research Laboratory under contract number W911NF-16-2-0189. The numerical simulations for this work were also carried out using the Extreme Science and Engineering Discovery Environment (XSEDE) see [97], which is supported by National Science Foundation grant number ACI-1548562. Through XSEDE we used the SDSC Expanse HPC resources, allocation identification DMS200031.

REFERENCES

- [1] E. ALBERDI, M. V. SÁNCHEZ-GÓMEZ, F. CAVALIERE, A. PÉREZ-SAMARTÍN, J. L. ZUGAZA, R. TRULLAS, M. DOMERCQ, AND C. MATUTE, *Amyloid β oligomers induce ca_2+ dysregulation and neuronal death through activation of ionotropic glutamate receptors*, Cell calcium, 47 (2010), pp. 264–272.
- [2] G. ALBI AND L. PARESCHI, *High order semi-implicit multistep methods for time-dependent partial differential equations*, Communications on Applied Mathematics and Computation, 3 (2021), pp. 701–718, <https://doi.org/10.1007/s42967-020-00110-5>, <https://doi.org/10.1007/s42967-020-00110-5>.
- [3] G. A. ASCOLI, D. E. DONOHUE, AND M. HALAVI, *NeuroMorpho.org: A central resource for neuronal morphologies*, Journal of Neuroscience, 27 (2007), pp. 9247–9251, <https://doi.org/10.1523/jneurosci.2055-07.2007>, <https://doi.org/10.1523/jneurosci.2055-07.2007>.
- [4] M. J. BERRIDGE, *Neuronal calcium signaling*, Neuron, 21 (1998), pp. 13–26.
- [5] M. J. BERRIDGE, M. D. BOOTMAN, AND H. L. RODERICK, *Calcium signalling: dynamics, homeostasis and remodelling*, Nature reviews Molecular cell biology, 4 (2003), pp. 517–529.
- [6] M. J. BERRIDGE, P. LIPP, AND M. D. BOOTMAN, *The versatility and universality of calcium signalling*, Nature reviews Molecular cell biology, 1 (2000), pp. 11–21.
- [7] Z. BERTELS, H. SINGH, I. DRIPPS, K. SIEGERSMA, A. F. TIPTON, W. D. WITKOWSKI, Z. SHEETS, P. SHAH, C. CONWAY, E. MANGUTOV, M. AO, V. PETUKHOVA, B. KARUMUDI, P. A. PETUKHOV, S. M. BACA, M. M. RASENICK, AND A. A. PRADHAN, *Neuronal complexity is attenuated in preclinical models of migraine and restored by HDAC6 inhibition*, eLife, 10 (2021), <https://doi.org/10.7554/elife.63076>, <https://doi.org/10.7554/elife.63076>.
- [8] L. J. BORG-GRAHAM, *Interpretations of Data and Mechanisms for Hippocampal Pyramidal Cell Models*, Springer US, Boston, MA, 1999, pp. 19–138, https://doi.org/10.1007/978-1-4615-4903-1_2, https://doi.org/10.1007/978-1-4615-4903-1_2.
- [9] P. BOROLE, *Calciumsim: Simulator for calcium dynamics on neuron graphs using dimensionally reduced model*, 2022, <https://doi.org/10.34944/DSPACE/7643>, <https://scholarshare.temple.edu/handle/20.500.12613/7671>.
- [10] T. BRANCO, B. A. CLARK, AND M. HÄUSSER, *Dendritic discrimination of temporal input sequences in cortical neurons*, Science, 329 (2010), pp. 1671–1675.
- [11] M. BREIT, M. KESSLER, M. STEPNIWSKI, A. VLACHOS, AND G. QUEISSER, *Spine-to-dendrite calcium modeling discloses relevance for precise positioning of ryanodine receptor-containing spine endoplasmic reticulum*, Scientific Reports, 8 (2018), <https://doi.org/10.1038/s41598-018-33343-9>, <https://doi.org/10.1038/s41598-018-33343-9>.
- [12] M. BREIT AND G. QUEISSER, *What is required for neuronal calcium waves? a numerical parameter study*, The Journal of Mathematical Neuroscience, 8 (2018), <https://doi.org/10.1186/s13408-018-0064-x>, <https://doi.org/10.1186/s13408-018-0064-x>.
- [13] M. BRINI AND E. CARAFOLI, *The plasma membrane ca_2+ atpase and the plasma membrane sodium calcium exchanger cooperate in the regulation of cell calcium*, Cold Spring Harbor perspectives in biology, 3 (2011), p. a004168.
- [14] M. M. CALBI, M. W. COLE, S. M. GATICA, M. J. BOJAN, AND G. STAN, *Condensed phases of gases inside nanotube bundles*, Reviews of Modern Physics, 73 (2001), p. 857.
- [15] E. CARAFOLI, *The role of mitochondria in the contraction-relaxation cycle and other ca_2+ -dependent activities of heart cells.*, Recent Advances in Studies on Cardiac Structure and Metabolism, 5 (1975), pp. 151–163.

- [16] A. C. CHARLES, S. K. KODALI, AND R. F. TYNDALE, *Intercellular calcium waves in neurons*, Molecular and Cellular Neuroscience, 7 (1996), pp. 337–353.
- [17] D. CRAPPER MCLACHLAN, L. WONG, C. BERGERON, AND K. BAIMBRIDGE, *Calmodulin and calbindin d28k in alzheimer disease*, Alzheimer Disease and Associated Disorders, 1 (1987), pp. 171–179.
- [18] D. D. DAVE AND B. K. JHA, *Mathematical modeling of calcium oscillatory patterns in a neuron*, Interdisciplinary Sciences: Computational Life Sciences, 13 (2021), pp. 12–24.
- [19] J. DE CALUWÉ AND G. DUPONT, *The progression towards alzheimer’s disease described as a bistable switch arising from the positive loop between amyloids and ca^{2+}* , Journal of theoretical biology, 331 (2013), pp. 12–18.
- [20] K. DEISSEROTH, P. G. MERMELSTEIN, H. XIA, AND R. W. TSIEN, *Signaling from synapse to nucleus: the logic behind the mechanisms*, Current opinion in neurobiology, 13 (2003), pp. 354–365.
- [21] S. T. DEKOSKY, S. W. SCHEFF, AND S. D. STYREN, *Structural correlates of cognition in dementia: quantification and assessment of synapse change*, Neurodegeneration, 5 (1996), pp. 417–421.
- [22] A. DEMURO, I. PARKER, AND G. E. STUTZMANN, *Calcium signaling and amyloid toxicity in alzheimer disease*, Journal of Biological Chemistry, 285 (2010), pp. 12463–12468.
- [23] A. DEMURO, M. SMITH, AND I. PARKER, *Single-channel ca^{2+} imaging implicates $a\beta_{1-42}$ amyloid pores in alzheimer’s disease pathology*, Journal of Cell Biology, 195 (2011), pp. 515–524.
- [24] J. DI CAPITE, S. W. NG, AND A. B. PAREKH, *Decoding of cytoplasmic ca^{2+} oscillations through the spatial signature drives gene expression*, Current Biology, 19 (2009), pp. 853–858.
- [25] C. DI SCALA, H. CHAHINIAN, N. YAHY, N. GARMY, AND J. FANTINI, *Interaction of alzheimer’s β -amyloid peptides with cholesterol: mechanistic insights into amyloid pore formation*, Biochemistry, 53 (2014), pp. 4489–4502.
- [26] C. DI SCALA, N. YAHY, S. BOUTEMEUR, A. FLORES, L. RODRIGUEZ, H. CHAHINIAN, AND J. FANTINI, *Common molecular mechanism of amyloid pore formation by alzheimer’s β -amyloid peptide and α -synuclein*, Scientific reports, 6 (2016), pp. 1–10.
- [27] R. E. DOLMETSCH, R. S. LEWIS, C. C. GOODNOW, AND J. I. HEALY, *Differential activation of transcription factors induced by ca^{2+} response amplitude and duration*, Nature, 386 (1997), pp. 855–858.
- [28] R. E. DOLMETSCH, K. XU, AND R. S. LEWIS, *Calcium oscillations increase the efficiency and specificity of gene expression*, Nature, 392 (1998), pp. 933–936.
- [29] G. DUPONT, M. FALCKE, V. KIRK, AND J. SNEYD, *The calcium toolbox*, in Models of Calcium Signalling, Springer, 2016, pp. 29–96.
- [30] D. M. EGELMAN AND P. R. MONTAGUE, *Calcium dynamics in the extracellular space of mammalian neural tissue*, Biophysical journal, 76 (1999), pp. 1856–1867.
- [31] D. FUTAGI AND K. KITANO, *Ryanodine-receptor-driven intracellular calcium dynamics underlying spatial association of synaptic plasticity*, Journal of computational neuroscience, 39 (2015), pp. 329–347.
- [32] D. GIL, A. H. GUSE, AND G. DUPONT, *Three-dimensional model of sub-plasmalemmal ca^{2+} microdomains evoked by the interplay between *orai1* and *insp3* receptors*, Frontiers in immunology, 12 (2021).
- [33] M. GRAUPNER, *A theory of plasma membrane calcium pump function and its consequences for presynaptic calcium dynamics*, Dissertation and Theses, (2003).
- [34] M. GRAUPNER, F. ERLER, AND M. MEYER-HERMANN, *A theory of plasma membrane calcium pump stimulation and activity*, Journal of Biological Physics, 31 (2005), pp. 183–206, <https://doi.org/10.1007/s10867-005-4472-2>, <https://doi.org/10.1007/s10867-005-4472-2>.
- [35] K. N. GREEN AND F. M. LAFERLA, *Linking calcium to $a\beta$ and alzheimer’s disease*, Neuron, 59 (2008), pp. 190–194.
- [36] P. L. GREER AND M. E. GREENBERG, *From synapse to nucleus: calcium-dependent gene transcription in the control of synapse development and function*, Neuron, 59 (2008), pp. 846–860.
- [37] S. GREIN, M. STEPNIIEWSKI, S. REITER, M. M. KNODEL, AND G. QUEISSER, *1d-3d hybrid modeling from multi-compartment models to full resolution models in space and time*, Frontiers in Neuroinformatics, 8 (2014), <https://doi.org/10.3389/fninf.2014.00068>, <https://doi.org/10.3389/fninf.2014.00068>.
- [38] A. M. HAGENSTON AND H. BADING, *Calcium signaling in synapse-to-nucleus communication*, Cold Spring Harbor perspectives in biology, 3 (2011), p. a004564.
- [39] G. E. HARDINGHAM, *Synapse-to-nucleus calcium signalling*, Molecular Biology of the Neuron

- (Molecular and Cellular Neurobiology), (2004), p. 249.
- [40] E. R. HIGGINS, M. B. CANNELL, AND J. SNEYD, *A buffering serca pump in models of calcium dynamics*, Biophysical journal, 91 (2006), pp. 151–163.
- [41] A. L. HODGKIN AND A. F. HUXLEY, *The components of membrane conductance in the giant axon of loligo*, The Journal of Physiology, 116 (1952), pp. 473–496, <https://doi.org/10.1113/jphysiol.1952.sp004718>, <https://doi.org/10.1113/jphysiol.1952.sp004718>.
- [42] A. L. HODGKIN AND A. F. HUXLEY, *Currents carried by sodium and potassium ions through the membrane of the giant axon of loligo*, The Journal of Physiology, 116 (1952), pp. 449–472, <https://doi.org/10.1113/jphysiol.1952.sp004717>, <https://doi.org/10.1113/jphysiol.1952.sp004717>.
- [43] A. L. HODGKIN AND A. F. HUXLEY, *The dual effect of membrane potential on sodium conductance in the giant axon of loligo*, The Journal of Physiology, 116 (1952), pp. 497–506, <https://doi.org/10.1113/jphysiol.1952.sp004719>, <https://doi.org/10.1113/jphysiol.1952.sp004719>.
- [44] A. L. HODGKIN AND A. F. HUXLEY, *A quantitative description of membrane current and its application to conduction and excitation in nerve*, The Journal of Physiology, 117 (1952), pp. 500–544, <https://doi.org/10.1113/jphysiol.1952.sp004764>, <https://doi.org/10.1113/jphysiol.1952.sp004764>.
- [45] A. L. HODGKIN, A. F. HUXLEY, AND B. KATZ, *Measurement of current-voltage relations in the membrane of the giant axon of loligo*, The Journal of Physiology, 116 (1952), pp. 424–448, <https://doi.org/10.1113/jphysiol.1952.sp004716>, <https://doi.org/10.1113/jphysiol.1952.sp004716>.
- [46] A. M. IACOPINO AND S. CHRISTAKOS, *Specific reduction of calcium-binding protein (28-kilodalton calbindin-d) gene expression in aging and neurodegenerative diseases.*, Proceedings of the National Academy of Sciences, 87 (1990), pp. 4078–4082.
- [47] A. ITKIN, V. DUPRES, Y. F. DUFRE'NE, B. BECHINGER, J.-M. RUYSSCHAERT, AND V. RAUSSENS, *Calcium ions promote formation of amyloid β -peptide (1–40) oligomers causally implicated in neuronal toxicity of alzheimer's disease*, PloS one, 6 (2011), p. e18250.
- [48] L. F. JAFFE, *Stretch-activated calcium channels relay fast calcium waves propagated by calcium-induced calcium influx*, Biology of the Cell, 99 (2007), pp. 175–184.
- [49] B. C. KARISSETTY, A. BHATNAGAR, E. M. ARMOUR, M. BEAVER, H. ZHANG, AND F. ELEFANT, *Amyloid- β peptide impact on synaptic function and neuroepigenetic gene control reveal new therapeutic strategies for alzheimer's disease*, Frontiers in molecular neuroscience, 13 (2020), p. 577622.
- [50] G. KASHYAP, D. BAPAT, D. DAS, R. GOWAIKAR, R. AMRITKAR, G. RANGARAJAN, V. RAVINDRANATH, AND G. AMBIKA, *Synapse loss and progress of alzheimer's disease-a network model*, Scientific Reports, 9 (2019), p. 6555.
- [51] M. KAWAHARA, *Disruption of calcium homeostasis in the pathogenesis of alzheimer's disease and other conformational diseases*, Current Alzheimer Research, 1 (2004), pp. 87–95.
- [52] M. KAWAHARA, N. ARISPE, Y. KURODA, AND E. ROJAS, *Alzheimer's disease amyloid beta-protein forms zn (2+)-sensitive, cation-selective channels across excised membrane patches from hypothalamic neurons*, Biophysical journal, 73 (1997), pp. 67–75.
- [53] J. KEIZER AND L. LEVINE, *Ryanodine receptor adaptation and ca^{2+} induced ca^{2+} release-dependent ca^{2+} oscillations*, Biophysical Journal, 71 (1996), pp. 3477–3487, [https://doi.org/10.1016/s0006-3495\(96\)79543-7](https://doi.org/10.1016/s0006-3495(96)79543-7), [https://doi.org/10.1016/s0006-3495\(96\)79543-7](https://doi.org/10.1016/s0006-3495(96)79543-7).
- [54] C. KOCH AND I. SEGEV, *Methods in Neuronal Modeling: From Synapses to Networks*, A Bradford book, MIT Press, 1989, <https://books.google.com/books?id=INvIQwAACAAJ>.
- [55] S. KOOK, H. JEONG, M. KANG, R. PARK, H. SHIN, S. HAN, S. SON, H. SONG, S. BAIK, M. MOON, E. YI, D. HWANG, AND I. MOOK-JUNG, *Crucial role of calbindin-d28k in the pathogenesis of alzheimer's disease mouse model*, Cell Death & Differentiation, 21 (2014), pp. 1575–1587.
- [56] S. KUPZIG, S. A. WALKER, AND P. J. CULLEN, *The frequencies of calcium oscillations are optimized for efficient calcium-mediated activation of ras and the erk/mapk cascade*, Proceedings of the National Academy of Sciences, 102 (2005), pp. 7577–7582.
- [57] R. LAL, H. LIN, AND A. P. QUIST, *Amyloid beta ion channel: 3d structure and relevance to amyloid channel paradigm*, Biochimica et Biophysica Acta (BBA)-Biomembranes, 1768 (2007), pp. 1966–1975.
- [58] A. T. LANDAU, P. PARK, J. D. WONG-CAMPOS, H. TIAN, A. E. COHEN, AND B. L. SABATINI, *Dendritic branch structure compartmentalizes voltage-dependent calcium influx in cortical layer 2/3 pyramidal cells*, eLife, 11 (2022), p. e76993, <https://doi.org/10.7554/eLife.76993>, <https://doi.org/10.7554/eLife.76993>.

- [59] M. E. LARKUM, S. WATANABE, T. NAKAMURA, N. LASSER-ROSS, AND W. N. ROSS, *Synaptically activated ca_2+ waves in layer 2/3 and layer 5 rat neocortical pyramidal neurons*, The Journal of Physiology, 549 (2003), pp. 471–488.
- [60] J. LATULIPPE, D. LOTITO, AND D. MURBY, *A mathematical model for the effects of amyloid beta on intracellular calcium*, PloS one, 13 (2018), p. e0202503.
- [61] R. J. LEVEQUE, *Finite Difference Methods for Ordinary and Partial Differential Equations*, Society for Industrial and Applied Mathematics, Jan. 2007, <https://doi.org/10.1137/1.9780898717839>, <https://doi.org/10.1137/1.9780898717839>.
- [62] W.-H. LI, J. LLOPIS, M. WHITNEY, G. ZLOKARNIK, AND R. Y. TSIEN, *Cell-permeant caged $insp_3$ ester shows that ca_2+ spike frequency can optimize gene expression*, Nature, 392 (1998), pp. 936–941.
- [63] H. LIN, Y. J. ZHU, AND R. LAL, *Amyloid β protein (1- 40) forms calcium-permeable, zn_2+ -sensitive channel in reconstituted lipid vesicles*, Biochemistry, 38 (1999), pp. 11189–11196.
- [64] C. LOHMANN AND R. O. WONG, *Regulation of dendritic growth and plasticity by local and global calcium dynamics*, Cell calcium, 37 (2005), pp. 403–409.
- [65] P. MARAMBAUD, U. DRESES-WERRINGLOER, AND V. VINGTDEUX, *Calcium signaling in neurodegeneration*, Molecular neurodegeneration, 4 (2009), pp. 1–15.
- [66] J. MARSH AND P. ALIFRAGIS, *Synaptic dysfunction in alzheimer’s disease: the effects of amyloid beta on synaptic vesicle dynamics as a novel target for therapeutic intervention*, Neural regeneration research, 13 (2018), p. 616.
- [67] M. P. MATTSON, *Calcium and neurodegeneration*, Aging cell, 6 (2007), pp. 337–350.
- [68] E. MCIVOR, S. COOMBES, AND R. THUL, *Three-dimensional spatio-temporal modelling of store operated ca_2+ entry: Insights into er refilling and the spatial signature of ca_2+ signals*, Cell calcium, 73 (2018), pp. 11–24.
- [69] K. MICHAELSEN AND C. LOHMANN, *Calcium dynamics at developing synapses: mechanisms and functions*, European Journal of Neuroscience, 32 (2010), pp. 218–223.
- [70] L. MILLER, J. J. PETROZZINO, G. GOLARAI, AND J. A. CONNOR, *Ca_2+ release from intracellular stores induced by afferent stimulation of ca_3 pyramidal neurons in hippocampal slices*, Journal of neurophysiology, 76 (1996), pp. 554–562.
- [71] J. J. PALOP, B. JONES, L. KEKONIUS, J. CHIN, G.-Q. YU, J. RABER, E. MASLIAH, AND L. MUCKE, *Neuronal depletion of calcium-dependent proteins in the dentate gyrus is tightly linked to alzheimer’s disease-related cognitive deficits*, Proceedings of the National Academy of Sciences, 100 (2003), pp. 9572–9577.
- [72] A. B. PAREKH AND J. W. PUTNEY JR, *Store-operated calcium channels*, Physiological reviews, 85 (2005), pp. 757–810.
- [73] J. B. PARYS AND G. BULTYNCK, *Calcium signaling in health, disease and therapy*, 2018.
- [74] H. B. POLLARD, E. ROJAS, AND N. ARISPE, *A new hypothesis for the mechanism of amyloid toxicity, based on the calcium channel activity of amyloid β protein ($a\beta p$) in phospholipid bilayer membranes*, Annals of the New York Academy of Sciences, 695 (1993), pp. 165–168.
- [75] M. POSPISCHIL, M. TOLEDO-RODRIGUEZ, C. MONIER, Z. PIWKOWSKA, T. BAL, Y. FRÉGNAC, H. MARKRAM, AND A. DESTEXHE, *Minimal hodgkin-huxley type models for different classes of cortical and thalamic neurons*, Biological Cybernetics, 99 (2008), pp. 427–441, <https://doi.org/10.1007/s00422-008-0263-8>, <https://doi.org/10.1007/s00422-008-0263-8>.
- [76] A. PROTOPAPAS, M. VANIER, AND J. BOWER, *Simulating large networks of neurons*, in Methods in Neuronal Modeling: From Synapses to Networks, MIT Press, 01 1998, pp. 461–498.
- [77] J. W. PUTNEY, N. STEINCKWICH-BESANÇON, T. NUMAGA-TOMITA, F. M. DAVIS, P. N. DESAI, D. M. D’AGOSTIN, S. WU, AND G. S. BIRD, *The functions of store-operated calcium channels*, Biochimica et Biophysica Acta (BBA)-Molecular Cell Research, 1864 (2017), pp. 900–906.
- [78] A. QUIST, I. DOUDEVSKI, H. LIN, R. AZIMOVA, D. NG, B. FRANGIONE, B. KAGAN, J. GHISO, AND R. LAL, *Amyloid ion channels: a common structural link for protein-misfolding disease*, Proceedings of the National Academy of Sciences, 102 (2005), pp. 10427–10432.
- [79] L. REDMOND AND A. GHOSH, *Regulation of dendritic development by calcium signaling*, Cell calcium, 37 (2005), pp. 411–416.
- [80] J. ROSADO, V. D. BUI, C. A. HAAS, J. BECK, G. QUEISSER, AND A. VLACHOS, *Calcium modeling of spine apparatus-containing human dendritic spines demonstrates an “all-or-nothing” communication switch between the spine head and dendrite*, PLOS Computational Biology, 18 (2022), p. e1010069, <https://doi.org/10.1371/journal.pcbi.1010069>, <https://doi.org/10.1371/journal.pcbi.1010069>.
- [81] J. M. ROSADO, *Ultrastructural neuronal modeling of calcium dynamics under transcranial magnetic stimulation*, 2022, <https://doi.org/10.34944/DSPACE/8010>, <https://doi.org/10.34944/DSPACE/8010>, <https://doi.org/10.34944/DSPACE/8010>.

- scholarshare.temple.edu/handle/20.500.12613/8038.
- [82] W. N. ROSS, *Understanding calcium waves and sparks in central neurons*, Nature Reviews Neuroscience, 13 (2012), pp. 157–168.
 - [83] B. SEIBOLD, D. SHIROKOFF, AND D. ZHOU, *Unconditional stability for multistep ImEx schemes: Practice*, J. Comput. Phys., 376 (2019), pp. 295–321.
 - [84] G. M. SHANKAR AND D. M. WALSH, *Alzheimer's disease: synaptic dysfunction and $\alpha\beta$* , Molecular neurodegeneration, 4 (2009), pp. 1–13.
 - [85] V. M. SHKRYL, *The spatio-temporal properties of calcium transients in hippocampal pyramidal neurons in vitro*, Frontiers in Cellular Neuroscience, 16 (2022), p. 1054950.
 - [86] A. SHTIFMAN, C. W. WARD, D. R. LAVER, M. L. BANNISTER, J. R. LOPEZ, M. KITAZAWA, F. M. LAFERLA, N. IKEMOTO, AND H. W. QUERFURTH, *Amyloid- β protein impairs ca^{2+} release and contractility in skeletal muscle*, Neurobiology of aging, 31 (2010), pp. 2080–2090.
 - [87] S. L. SMITH, I. T. SMITH, T. BRANCO, AND M. HÄUSSER, *Dendritic spikes enhance stimulus selectivity in cortical neurons in vivo*, Nature, 503 (2013), pp. 115–120.
 - [88] J. SNEYD, K. TSANEVA-ATANASOVA, J. BRUCE, S. STRAUB, D. GIOVANNUCCI, AND D. YULE, *A model of calcium waves in pancreatic and parotid acinar cells*, Biophysical Journal, 85 (2003), pp. 1392–1405, [https://doi.org/10.1016/s0006-3495\(03\)74572-x](https://doi.org/10.1016/s0006-3495(03)74572-x), [https://doi.org/10.1016/s0006-3495\(03\)74572-x](https://doi.org/10.1016/s0006-3495(03)74572-x).
 - [89] T. L. SPIRES-JONES AND B. T. HYMAN, *The intersection of amyloid beta and tau at synapses in alzheimer's disease*, Neuron, 82 (2014), pp. 756–771.
 - [90] E. STOCKLEY, H. COLE, A. BROWN, AND H. WHEAL, *A system for quantitative morphological measurement and electrotonic modelling of neurons: three-dimensional reconstruction*, Journal of Neuroscience Methods, 47 (1993), pp. 39–51, [https://doi.org/10.1016/0165-0270\(93\)90020-r](https://doi.org/10.1016/0165-0270(93)90020-r), [https://doi.org/10.1016/0165-0270\(93\)90020-r](https://doi.org/10.1016/0165-0270(93)90020-r).
 - [91] J. SUBRAMANIAN, J. C. SAVAGE, AND M.-É. TREMBLAY, *Synaptic loss in alzheimer's disease: mechanistic insights provided by two-photon in vivo imaging of transgenic mouse models*, Frontiers in Cellular Neuroscience, (2020), p. 445.
 - [92] D. J. SURMEIER, *Calcium, ageing, and neuronal vulnerability in parkinson's disease*, The Lancet Neurology, 6 (2007), pp. 933–938.
 - [93] D. ŚWIETLIK, J. BIAŁOWKAS, J. MORYŚ, AND A. KUSIAK, *Computer model of synapse loss during an alzheimer's disease-like pathology in hippocampal subregions dg, ca3 and ca1—the way to chaos and information transfer*, Entropy, 21 (2019), p. 408.
 - [94] R. D. TERRY, E. MASLIAH, D. P. SALMON, N. BUTTERS, R. DETERESA, R. HILL, L. A. HANSEN, AND R. KATZMAN, *Physical basis of cognitive alterations in alzheimer's disease: synapse loss is the major correlate of cognitive impairment*, Annals of Neurology: Official Journal of the American Neurological Association and the Child Neurology Society, 30 (1991), pp. 572–580.
 - [95] Y. TIMOFEEVA, G. J. LORD, AND S. COOMBES, *Dendritic cable with active spines: A modelling study in the spike-diffuse-spike framework*, Neurocomputing, 69 (2006), pp. 1058–1061.
 - [96] A. TINKER, A. R. G. LINDSAY, AND A. J. WILLIAMS, *Cation conduction in the calcium release channel of the cardiac sarcoplasmic reticulum under physiological and pathophysiological conditions*, Cardiovascular Research, 27 (1993), pp. 1820–1825, <https://doi.org/10.1093/cvr/27.10.1820>, <https://doi.org/10.1093/cvr/27.10.1820>.
 - [97] J. TOWNS, T. COCKERILL, M. DAHAN, I. FOSTER, K. GAITHER, A. GRIMSHAW, V. HAZLEWOOD, S. LATHROP, D. LIFKA, G. D. PETERSON, R. ROSKIES, J. R. SCOTT, AND N. WILKINS-DIEHR, *Xsede: Accelerating scientific discovery*, Computing in Science & Engineering, 16 (2014), pp. 62–74, <https://doi.org/10.1109/MCSE.2014.80>.
 - [98] S. TU, S.-I. OKAMOTO, S. A. LIPTON, AND H. XU, *Oligomeric $\alpha\beta$ -induced synaptic dysfunction in alzheimer's disease*, Molecular neurodegeneration, 9 (2014), pp. 1–12.
 - [99] A. VERKHRATSKY AND A. SHMIGOL, *Calcium-induced calcium release in neurones*, Cell calcium, 19 (1996), pp. 1–14.
 - [100] Y. ZHOU, M. TREBAK, AND D. L. GILL, *Calcium signals tune the fidelity of transcriptional responses*, Molecular cell, 58 (2015), pp. 197–199.